Density-driven unstable flows of miscible fluids in a Hele-Shaw cell

By J. FERNANDEZ[1], P. KUROWSKI[1], P. PETITJEANS[1]
AND E. MEIBURG[1,2]

[1]Laboratoire de Physique et Mécanique des Milieux Hétérogènes (LPMMH),
Ecole Supérieure de Physique et de Chimie Industrielles (ESPCI),
10, rue Vauquelin, 75231 Paris Cedex 05, France

[2]Department of Mechanical and Environmental Engineering,
University of California at Santa Barbara,
Santa Barbara, CA 93106, USA

Density-driven instabilities between miscible fluids in a vertical Hele-Shaw cell are investigated by means of experimental measurements, as well as two- and three-dimensional numerical simulations. The experiments focus on the early stages of the instability growth, and they provide detailed information regarding the growth rates and most amplified wavenumbers as a function of the governing Rayleigh number Ra. They identify two clearly distinct parameter regimes: a low-Ra, 'Hele-Shaw' regime in which the dominant wavelength scales as Ra^{-1}, and a high-Ra 'gap' regime in which the length scale of the instability is 5 ± 1 times the gap width. The experiments are compared to a recent linear stability analysis based on the Brinkman equation. The analytical dispersion relationship for a step-like density profile reproduces the experimentally observed trend across the entire Ra range. Nonlinear simulations based on the two- and three-dimensional Stokes equations indicate that the high-Ra regime is characterized by an instability across the gap, wheras in the low-Ra regime a spanwise Hele-Shaw mode dominates.

1. Introduction

Understanding the dynamical evolution of interfaces remains a key challenge in fluid dynamics research. While interfaces play a crucial role in a variety of instabilities vital to industrial processes, their dynamics also greatly influence more fundamental fields in different branches of science. Within the present article, our focus is on gravitationally unstable interfaces, i.e. interfaces that separate a lighter fluid from a heavier one located above it in a gravitational field. For fluid layers of large extent in the horizontal directions, both the linear and the nonlinear evolution of the ensuing, so-called Rayleigh–Taylor instability have been the subject of numerous investigations (e.g. Sharp 1984; Kurowski, Misbah & Tchourkine 1995). Less well understood is the evolution of this instability in a vertically arranged Hele-Shaw cell. Here the flow is dominated by viscous forces, while inertial forces are usually negligible. This is reflected by the small value of the Reynolds number $Re = Ue/v$, where U denotes a characteristic flow velocity, e represents the gap thickness of the cell, and v indicates the kinematic viscosity. Some insight into the stability characteristics of interfaces in such narrow cells has been gained from analyses of the gap-averaged, two-dimensional Hele-Shaw equations. Within this theoretical framework, Saffman & Taylor (1958) as

well as Chuoke, Van Meurs & Van der Poel (1959) analysed the interface separating two immiscible fluids. However, several experimental investigations since then have shown that the approach of averaging across the gap is approximately valid only for large values of the dimensionless surface tension (Park, Gorell & Homsy 1984; Maxworthy 1987). For smaller values, three-dimensional flow effects as well as the dynamics of the wetting layer left behind on the walls of the Hele-Shaw cell become increasingly important (Park & Homsy 1984; Schwartz 1986, cf. also Bretherton 1961), and the observed dominant wavelength deviates strongly from the value predicted by the gap-averaged theory. Frequently it is found that the wavelength scales with the width of the gap separating the walls of the Hele-Shaw apparatus. In spite of the above observations, fully nonlinear simulations based on the gap-averaged equations have been used with some success in investigations of the nonlinear interaction mechanisms among the evolving fingers (Tryggvason & Aref 1983; DeGregoria & Schwartz 1986, 1987; Meiburg & Homsy 1988).

A similar situation arises for miscible flows in Hele-Shaw cells, whose dynamics are generally less well understood than their immiscible counterparts. To some extent, the role of molecular diffusion in miscible flows corresponds to that of surface tension in immiscible ones, in that both determine a short-wave cutoff length, cf. also the review provided by Homsy (1987). For gravitationally unstable problems in the absence of a net flow, the governing dimensionless parameter is the Rayleigh number $Ra = Ue/D$, where D denotes the molecular diffusion coefficient and U represents a suitably defined buoyancy velocity. Few experiments have been performed on gravitationally unstable miscible fluids since the early work of Wooding (1969), who observed the growth of fingers at the diffusing interface between two fluids of identical viscosities. His experiments were conducted in a Hele-Shaw cell at high Ra values, and they showed the mean wavelength and the finger amplitude to grow proportionally to $t^{1/2}$ and t, respectively. For these large Ra, just as for large capillary number Ca, a wetting layer forms on the walls of the Hele-Shaw cell (Paterson 1985; Petitjeans & Maxworthy 1996; Chen & Meiburg 1996; Lajeuneese *et al.* 1997; Petitjeans *et al.* 1999). This indicates that the velocity profile across the gap is no longer parabolic, so that the Hele-Shaw equations cannot be expected to provide an accurate description of the flow. While the exact stability parameter value above which the Hele-Shaw equations are no longer applicable is at present unknown, for forced flows there exist estimates in the literature regarding the validity of the Hele-Shaw approach ranging from $O(10)$ (Yang & Yortsos 1997) to $O(100)$ (Chen & Meiburg 1996, cf. also Lajeunesse *et al.* 1999, 2001). It should be kept in mind that the exact value also depends on the viscosity ratio of the two fluids. The matter is further complicated by the fact that a truly steady state cannot develop in miscible flows (Chen & Meiburg 1996), and that eventually the flow in the gap will approach Taylor dispersion (Taylor 1953). Nevertheless, stability analyses (e.g. Tan & Homsy 1986; Rogerson & Meiburg 1993*a*) as well as numerical simulations (e.g. Tan & Homsy 1988; Manickam & Homsy 1993; Rogerson & Meiburg 1993*b*; Chen & Meiburg 1998*a*; Ruith & Meiburg 2000) based on the Hele-Shaw equations have been able to provide some insight into the dynamics of these flows.

The paper is organized as follows. In §2, the physical problem is described in more detail, and the relevant dimensionless parameters are identified. Subsequently, in §3 experimental measurements are reported of gravitationally unstable interfaces between miscible fluids in a Hele-Shaw cell. Data are provided regarding both the initial wavelength of the fingers and their growth rates over a large range of Ra. These data demonstrate the existence of a high-Ra regime that is clearly distinct from
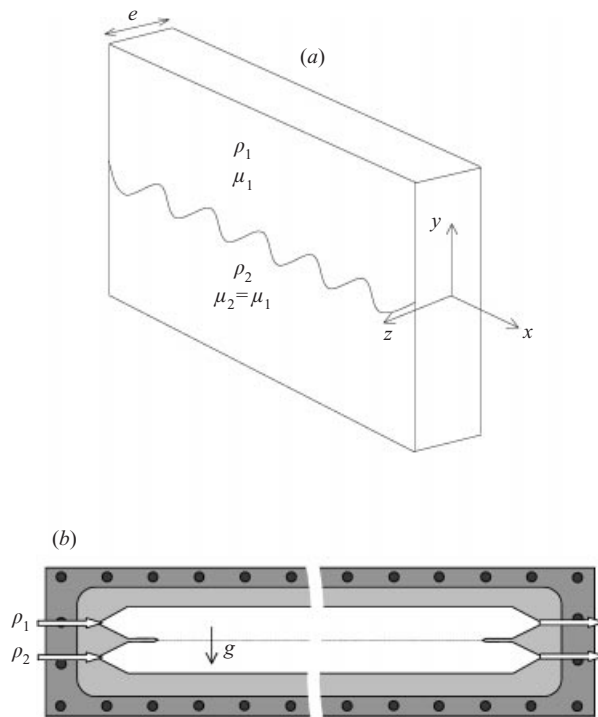
FIGURE 1. (*a*) Schematic view of the Hele-Shaw cell. (*b*) Experimental apparatus. The channel is divided into two sections each of which is 3 cm high and 53 cm long.

its low-Ra counterpart. These two Ra ranges are characterized by different scaling laws for the dominant instability wavelength. In §4, these experimental observations are compared with the results of a novel linear stability analysis (Fernandez *et al.* 2001) based on the Brinkman equation, which predict the correct scaling trend across the entire range of Ra values. Section 5 presents numerical simulations of the two- and three-dimensional Stokes equations. First, it is shown that the two-dimensional flow within the gap is stable for low Ra values, while for large Ra it gives rise to a so-called 'gap instability.' Subsequent three-dimensional simulations show that at low Ra the evolution in the spanwise direction is characterized by a Hele-Shaw instability mode, while at large Ra a three-dimensional variation of the gap instability mode dominates. Section 6 presents a few concluding remarks.

2. Physical problem, governing equations, and dimensionless parameters

Consider a narrow gap of width e between two vertical plates that is filled with two miscible fluids of equal viscosities but different densities, cf. figure 1(*a*). Initially the heavier fluid is situated on top of the lighter one, thereby giving rise to an unstable density stratification. Our interest focuses on the early, linear evolution of the ensuing instability. In order to establish the characteristic scales of the problem along with the relevant dimensionless parameters, we consider the usual Hele-Shaw equations. Since the experimentally observed velocities are very small, inertial terms in the momentum equation can safely be neglected. If we assume that the fluids are miscible in all

proportions, and that the molecular diffusion coefficient is constant, we obtain

$$\nabla \cdot \boldsymbol{u} = 0, \tag{2.1a}$$

$$\nabla p = \frac{\mu}{K}\boldsymbol{u} - \rho g \nabla y, \tag{2.1b}$$

$$\frac{\partial c}{\partial t} + \boldsymbol{u} \cdot \nabla c = D\nabla^2 c, \tag{2.1c}$$

where the permeability $K = e^2/12$ and μ is viscosity. The above set of equations expresses the conservation of mass, momentum, and species, with c denoting the concentration of the heavier fluid. Gravity is taken to act in the negative y-direction, with x indicating the spanwise direction, and z pointing in the direction of the narrow gap (cf. figure 1). The density ρ is taken to be a linear function of the concentration

$$\rho = \rho_2 + c(\rho_1 - \rho_2), \tag{2.2}$$

where the subscripts 1 and 2 denote the heavier and lighter fluids, respectively. In order to render the governing equations dimensionless, we take the gap width e as the characteristic length scale L^*. Together with the characteristic velocity scale

$$U^* = \frac{\Delta\rho\,g\,e^2}{12\mu}, \tag{2.3}$$

we thus obtain the time scale

$$T^* = \frac{12\mu}{\Delta\rho\,g\,e}. \tag{2.4}$$

Characteristic values for the pressure and the density are obtained as

$$P^* = \Delta\rho\,g\,e, \quad \rho^* = \Delta\rho. \tag{2.5}$$

Upon absorbing the constant term in the c, ρ-relationship into the pressure, the dimensionless set of governing equations takes the form

$$\nabla \cdot \boldsymbol{u} = 0, \tag{2.6a}$$

$$\nabla p = \boldsymbol{u} - c\nabla y, \tag{2.6b}$$

$$\frac{\partial c}{\partial t} + \boldsymbol{u} \cdot \nabla c = \frac{1}{Ra}\nabla^2 c, \tag{2.6c}$$

where the dimensionless Rayleigh number

$$Ra = \frac{\Delta\rho\,g\,e^3}{12D\mu} \tag{2.7}$$

nominally expresses the ratio of convective and diffusive transport in the concentration equation. Note that in the presence of net flow through the Hele-Shaw cell, this dimensionless parameter should be referred to as a Péclet number. For the present stability problem in the absence of net flow, however, it is more appropriate to call it a Rayleigh number. Results will also be discussed as function of the Atwood number

$$At = \frac{\rho_1 - \rho_2}{\rho_1 + \rho_2}. \tag{2.8}$$

It should be emphasized that this parameter does not appear independently during the process of rendering the governing equations dimensionless.

Concentration of glycerol (%)	$\rho\,(\text{g cm}^{-3})$	$\mu\,(\text{cP})$	$Sc = v/D$	$b\,(\text{mm})$	$At(\times 10^{-2})$					
0	1	1	1000	0.05	0.15 0.25 0.35 0.45 0.55 0.65 0.75 0.95 1.5 2.5 3.5 4.5 5.5					
—	—	—	—	0.1	—					
—	—	—	—	0.15	—					
—	—	—	—	0.3	—					
—	—	—	—	0.5	—					
—	—	—	—	0.8	—					
—	—	—	—	1	—					
50	1.12	5	4.5×10^4	0.5	0.35 0.45 0.55 0.65 0.75 0.95 1.5 2.5					
—	—	—	—	1	—					
70	1.17	20	1.7×10^6	0.5	—					
—	—	—	—	1	—					

TABLE 1. Experimental parameters.

3. Experiments

3.1. *Set-up*

The experiments were conducted in a vertically arranged, rectangular Hele-Shaw cell formed by two 1 cm thick, tempered glass plates of 60 cm length and 12 cm width (figure 1*b*). The flow channel is cut from a millar sheet that maintains constant distance between the two plates. A metallic frame supports the two plates and the millar sheet, with uniform pressure along the cell in order to maintain a constant thickness with high accuracy, while avoiding leaks. The gap thickness e can be varied from 50 μm to 1 mm. The channel itself is 53 cm long and 6 cm wide. It has two inlets at one end, and two outlets at the opposite end. The channel ends are shaped specifically in order to minimize mixing between the two miscible fluids, and to establish a horizontal 'interface' of minimal thickness between them. The experimental procedure is as follows. Initially the entire cell is occupied by the lighter fluid. Subsequently, the two fluids are injected into the cell at identical flow rates by means of two identical glass syringes and a single syringe pump (the mean velocity in the cell is of the order of 5 cm s^{-1}). The lighter fluid enters through the lower inlet, while the heavier one is injected above it. After a few seconds, when a sharp interface has been established along the entire length of the cell, the pump is stopped, and simultaneously the inlets and outlets are closed. This defines the time $t_i = 0$ in our measurements. It should be pointed out that, although this configuration is gravitationally unstable, the characteristic time scale of the instability is significantly larger than the time needed to fill the cell, so that the interface is essentially level at time $t_i = 0$.

Experiments were conducted for the fluid combinations listed in table 1. The lighter of the two fluids consisted of pure water or a glycerine–water mixture. The heavier fluid was identical to the lighter one, except for some added red dye in the form of amaranth powder. The dye thus establishes the unstable density stratification, and it serves to visualize the ensuing instability. By varying the dye concentration, the Atwood number could be varied from 1.5×10^{-3} to 5.5×10^{-2}. The upper limit for At is established by the saturation concentration of the dye, which is approximately 3% in weight. Across the entire range of dye concentrations, the viscosity of the heavier fluid remained constant. The range of Rayleigh numbers that could be covered under these conditions extends across nearly five orders of magnitude from about 1 to
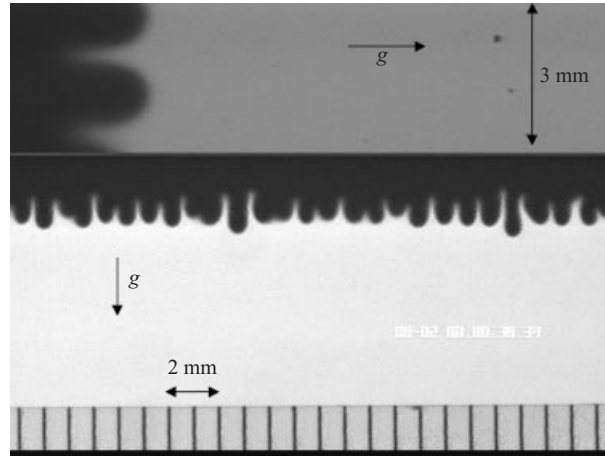
FIGURE 2. Two simultaneous views of the instability. The first image (upper part of the figure) shows one or two fingers growing from left to right. This image has a sufficiently fine resolution to allow us to measure the growth rate. The second image (lower part) captures many more fingers, so that the most amplified wavelength λ can be extracted.

almost 10^5. Consequently, the Reynolds number ($Re = Ra/Sc$) ranges from 10^{-4} to 10. However, even for Re values of 10, the convective terms are not expected to have much of an effect, as long as the flow in the gap remains nearly parallel.

3.2. *Measurement techniques*

Two CCD video cameras were employed to record the temporal development of the instability on the same video-tape (half an image for each camera), as shown in figure 2. The first video camera recorded a cell section of about 5 cm length containing many fingers, for the purpose of measuring a characteristic wavelength in the linear regime. The second camera took more detailed images of a smaller section a few mm in length that contained only one or two fingers, from which the growth rate of the instability could be deduced. A public domain image processing software package was employed in order to extract the coordinates of the interface from the images recorded by the first video camera. Here the interface location is defined by the $c = 0.5$ concentration isocontour (figure 3). Note that the interface thickness seems to decrease with time instead of increase. This is explained by the flow inside the finger, which brings some purer fluid to the tip of the finger, thereby rendering the concentration profile steeper (Petitjeans & Maxworthy 1996).

To each image, a discrete Fourier transformation was applied, in order to decompose the interfacial shape into its Fourier modes

$$A(x,t) = \sum_{m=0}^{N/2} A_m(t) \exp(\mathrm{i}k_m x) \tag{3.1}$$

with $k_m = 2\pi m/L$. $A(x,t)$ represents the position of the interface as a function of time t and horizontal coordinate x. $A_m(t)$ denotes the amplitude of mode k_m, L indicates the size of the image, and N represents the number of points. Figure 4 depicts a typical example of the Fourier modes at different time levels during the linear regime. The Fourier spectrum exhibits a dominant mode characterized by the highest amplitude
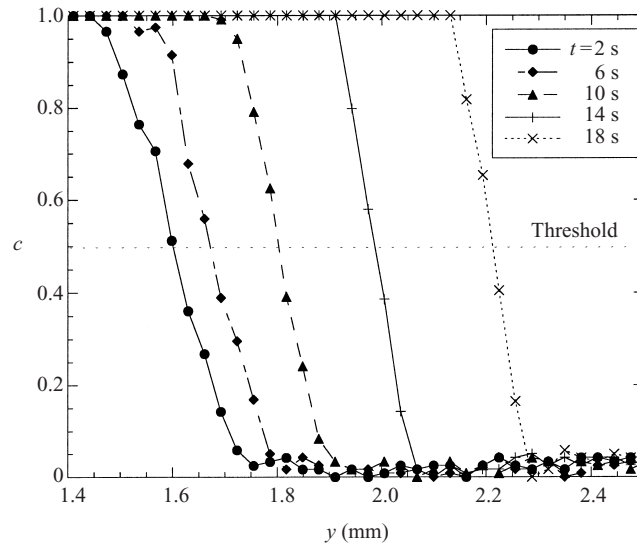
FIGURE 3. Evolution of the concentration profile with time at the tip of a finger. The interface position is tracked by applying a threshold at $c = 0.5$.
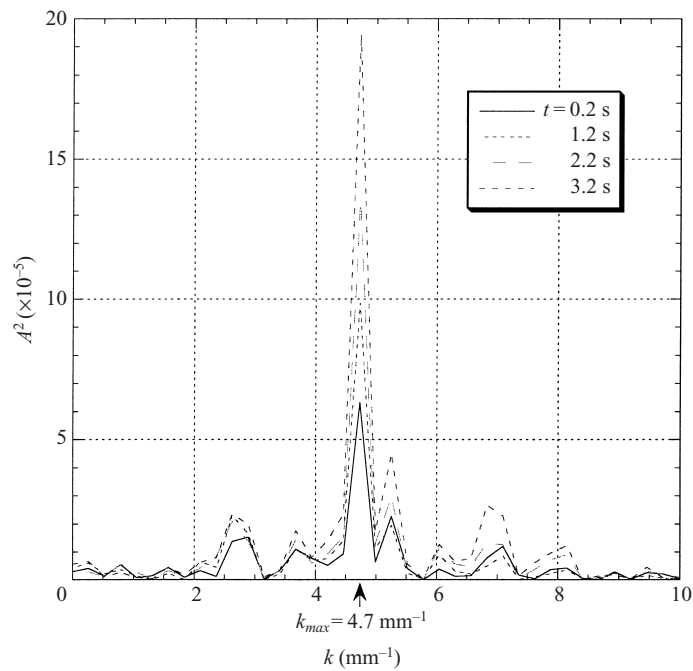

FIGURE 4. Characteristic Fourier spectrum of the interface evolution in the linear regime. The gap thickness e is $0.15\,\text{mm}$, and the Atwood number is 9.5×10^{-3}. The dominant wavenumber $k_{max} = 4.48\,\text{mm}^{-1}$ is constant at early times. The wavelength $\lambda \sim 9\,e$.

A_{max}. The growth rate $\Sigma(k_{max})$ of the dominant mode k_{max} is obtained from the relation

$$A_{max}(t) = a_o \exp(\Sigma(k_{max})t), \tag{3.2}$$

where a_o is a constant determined by the initial position of the interface. The growth
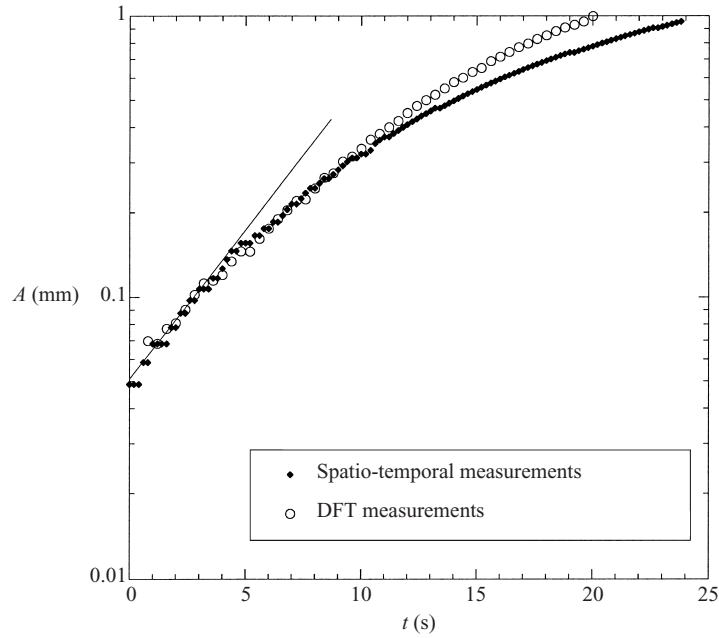
FIGURE 5. The growth rate Σ measured from a spatio-temporal diagram and a discrete Fourier transformation analysis. The measured values of Σ are similar: $\Sigma = 0.17\,\mathrm{s}^{-1}$.
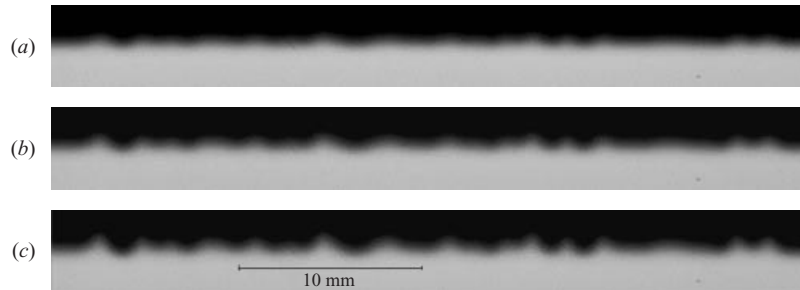

FIGURE 6. Photographs of the linear development of the interface for $Ra = 1.02$. (a) $t = 160\,\mathrm{s}$; (b) $t = 240\,\mathrm{s}$; (c) $t = 310\,\mathrm{s}$. The ratio λ/e is about 57.

rate Σ was also measured by analysing the early exponential growth of an individual finger tip amplitude $A_{tip}(t)$ from the images recorded by the second camera. As can be seen from figure 5, the growth rates measured by these two methods are similar in magnitude. One can clearly distinguish two separate regimes: during early times, the data points follow a straight line in this semi-log plot, indicating an exponential growth of the instability. At later times, the instability enters the nonlinear stages, which are beyond the scope of the present investigation. During this phase, the growth slows down, partly also due to the presence of the lower and upper boundaries of the cell, and the finger tip velocity approaches a constant value.

3.3. *Results*

3.3.1. *Qualitative observations*

Figures 6, 7 and 8 show the growth of the instability for the three different Ra values of 1, 26 and 250, respectively. For each value of Ra a pronounced interfacial
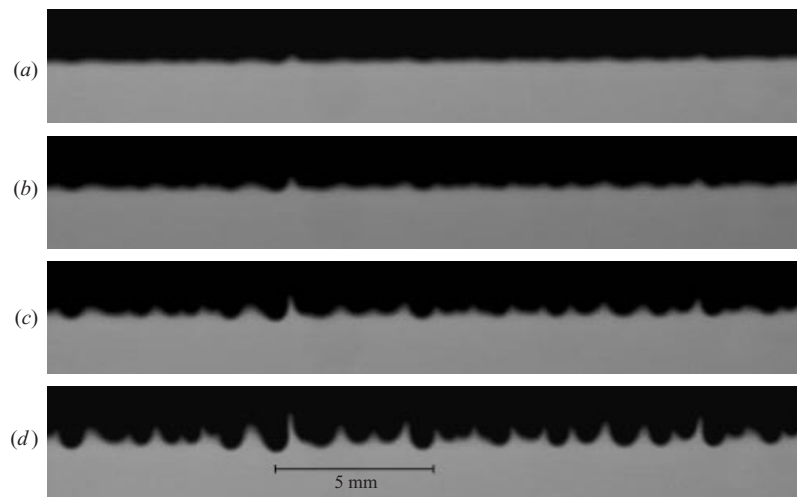
FIGURE 7. Photographs of the linear development of the interface for $Ra \simeq 26$. (a) $t = 0.4\,\text{s}$; (b) $t = 4\,\text{s}$; (c) $t = 8\,\text{s}$; (d) $t = 12\,\text{s}$. The ratio λ/e is approximately 9.
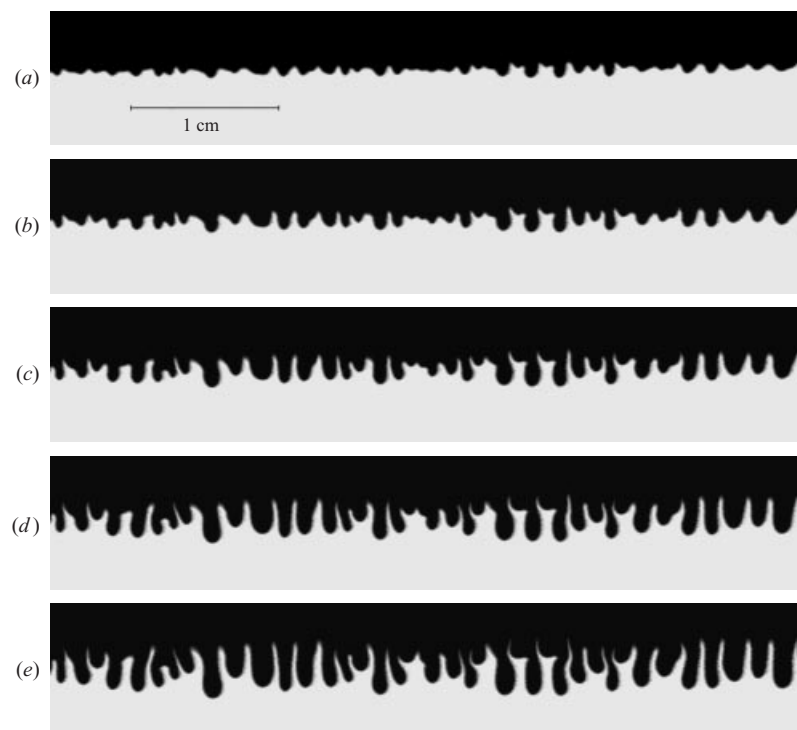

FIGURE 8. Photographs of the linear development of the interface for $Ra \simeq 250$. (a) $t = 0.6\,\text{s}$; (b) $t = 1.2\,\text{s}$; (c) $t = 1.8\,\text{s}$; (d) $t = 2.4\,\text{s}$; (e) $t = 3\,\text{s}$. The ratio λ/e is approximately 5.

waviness evolves, which subsequently grows into fingers. Due to experimental noise, there are slight differences between individual fingers, so that some of them grow more rapidly than others. However, all of them eventually reach large amplitudes. The average length as measured from the initial location of the interface is identical
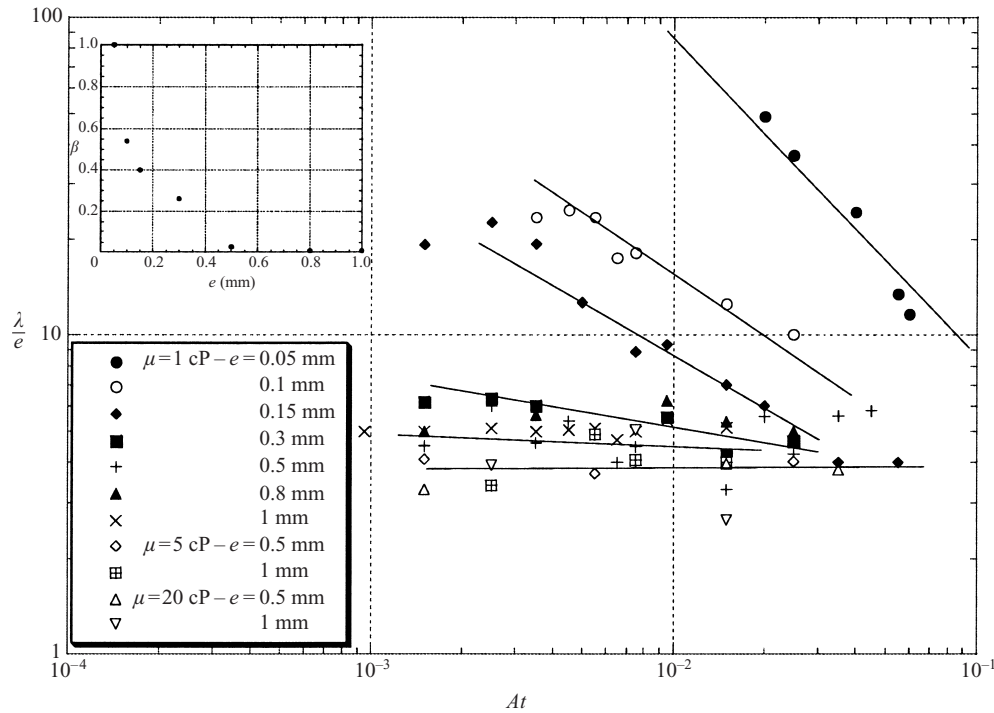
FIGURE 9. Experimental measurements of λ/e versus At.

for the heavier, falling fingers and the lighter, rising ones. This up–down symmetry is preserved as long as the two fluids have the same viscosity, in agreement with the findings by other authors (Tryggvason & Aref 1983; Maxworthy 1987). Even though these experiments were performed for identical fluid combinations, i.e. identical At values, the characteristic time scales for the formation of the fingers vary substantially with Ra (cf. §3.3.3). Throughout the linear regime, the dominant wavenumber is seen to remain constant with time for each of the different Ra values.

3.3.2. *Wavelength selection*

Quantitative measurements of the normalized characteristic wavelength λ/e during the early stages of finger formation are depicted in figures 9 and 10, as a function of At and Ra. The At dependence has the form of a power law, $\lambda/e \propto At^{-\beta}$ see inset to figure 9, where the exponent β decreases continuously from one to zero as the gap thickness e increases. When plotted as a function of Ra, all data points follow a similar trend that extends over nearly five orders of magnitude in Ra. This confirms the dominant role of Ra as the governing dimensionless parameter. Two distinct Ra regimes can be identified. For $Ra \leqslant 10$, the ratio λ/e scales as Ra^{-1}. In this regime, values of λ up to fifty times the gap width are measured for the smallest gap width of $e = 0.05$ mm. Under these circumstances diffusion is sufficiently strong to smooth out gradients across the gap, so that the scaling laws of the classical Hele-Shaw theory for miscible flows (Tan & Homsy 1986) apply. We refer to this parameter range as the low-Ra Hele-Shaw range.

For values of $Ra \geqslant 100$ the normalized wavelength is approximately constant, $\lambda/e = 5 \pm 1$. In this regime the wavelength shows no dependence on the density contrast between the two fluids. As we will see from the numerical results to be
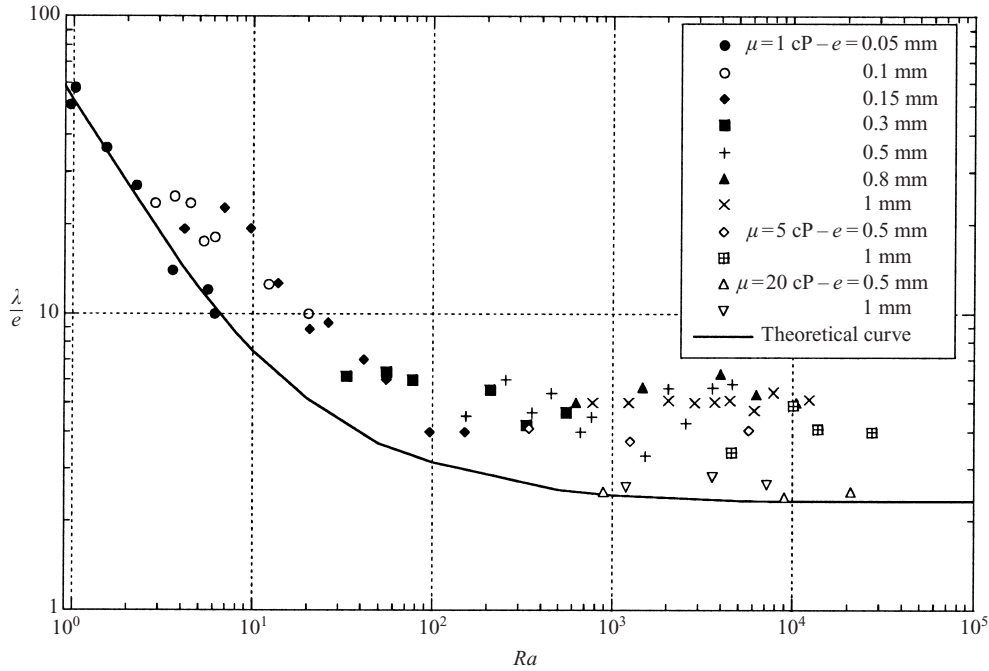
FIGURE 10. Experimental measurements of λ/e versus Ra. All data are seen to follow the same trend.

discussed below, at these large Ra values significant gradients across the gap can develop. The flow in this parameter range will be denoted as the high-Ra gap mode. The characteristic relationship between the wavelength λ and the gap e seen here is comparable to that found in other experiments with miscible fluids in Hele-Shaw cells, such as viscously driven instabilities (Paterson 1985; Lajeunesse *et al.* 1997, 1999; Maxworthy 1989), or even instabilities of immiscible fluid flows (e.g. §7 or Maxworthy 1989).

3.3.3. *Growth rate of the instability*

Figure 11 represents the dimensionless growth rate Σ as a function of Ra. For $Ra < 10$, it increases linearly with Ra, while for larger values of Ra it assumes a constant value near 0.3 ± 0.1. This confirms our earlier observation of two different parameter ranges governed by different physical transport processes, namely a small-Ra Hele-Shaw regime, and a large-Ra gap regime.

4. Comparison with linear stability results based on the Brinkman equation

In the following, we present a comparison with the linear stability analysis of Fernandez *et al.* (2001), which covers the entire range of Rayleigh numbers. It is based on the Brinkman equation (Brinkman 1947)

$$-\nabla p + \mu \Delta_{\parallel} \langle \boldsymbol{u} \rangle_z - \frac{12\mu}{e^2} \langle \boldsymbol{u} \rangle_z + \rho \boldsymbol{g} = 0, \tag{4.1}$$

which is commonly used to analyse flows in porous media of high porosity. Here $\Delta_{\parallel} = (\partial_{x^2} + \partial_{y^2})$ is the Laplace operator in the (x, y)-plane, and $\langle \boldsymbol{u} \rangle_z$ is the mean value
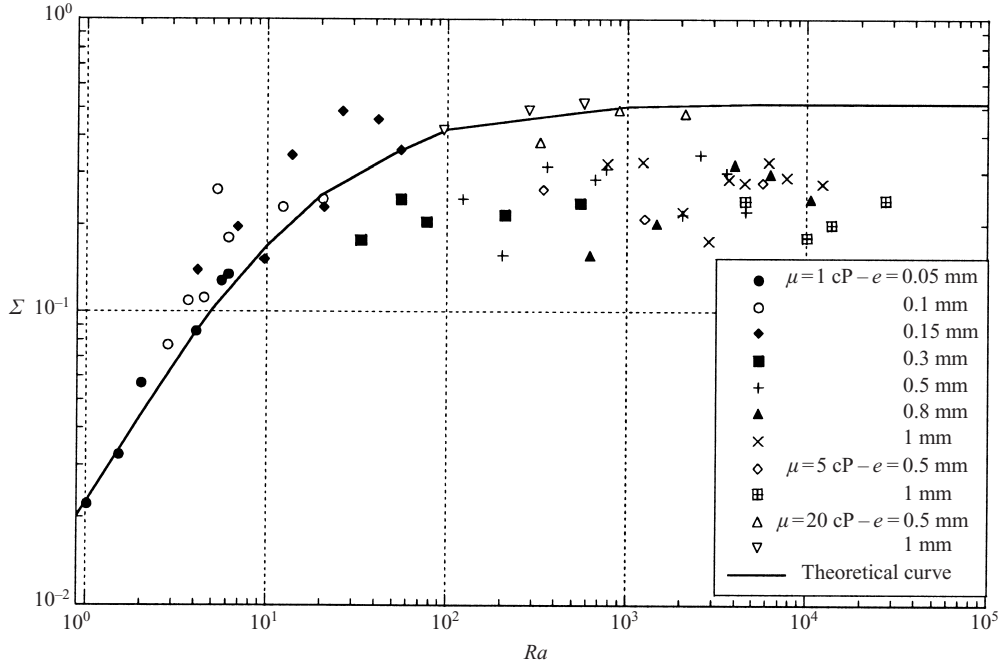
FIGURE 11. The non-dimensional growth rate Σ as a function of Ra. Two clearly distinct parameter regimes can be identified.

of $\boldsymbol{u}$ in the gap. For a step-like initial density profile, we obtain the dispersion relation

$$\Sigma = \frac{12}{Ra} + \frac{q}{2}\left[1 - \frac{q}{\sqrt{12+q^2}}\right] - \frac{6q}{Ra\Sigma}\left[1 - \frac{q}{\sqrt{q^2+Ra\Sigma}}\right], \qquad (4.2)$$

whose solutions are given in figure 12 for different Rayleigh numbers. The line in the graph represents the asymptotic dispersion relation for very large Ra. The maximum growth rate Σ_m and the corresponding wavenumber q_m can be deduced as a function of the Rayleigh number. They are represented in figures 10 and 11 with the experimental values. The stability results are seen to capture the correct trend across the entire Ra range. In particular, the results demonstrate that in the high-Ra regime the wavelength is selected only by the gap width, even though there is a quantitative discrepancy between the theoretical asymptotic value $\lambda/e = 2.3$ and the value of 5 ± 1 measured in the experiment. The difference between the theoretical and experimental asymptotic values may at least partially be due to the assumption of a Poiseuille base flow, which, as we will see from the numerical simulations to be discussed below, does not apply for the largest Ra data points. In figure 10, it can be observed that the measurements closest to the theoretical value are the ones obtained with the most viscous fluids, i.e. those cases for which the assumption of Poiseuille flow is most applicable. Note that this analysis can also be adapted to viscously driven instabilities, for which it has also been observed that at large Ra the wavelength scales only with the gap width.

In the low-Ra regime the dispersion relation (4.2) reduces to the classical dispersion relation derived for Darcy's law

$$\Sigma(q) = \tfrac{1}{2}\left(q - Ra^{-1}q^2 - Ra^{-1}q\sqrt{q^2+2Raq}\right). \qquad (4.3)$$
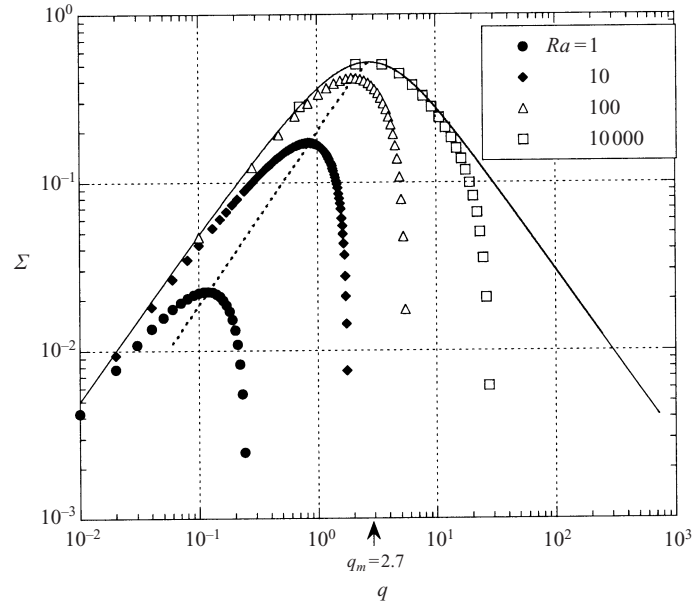
FIGURE 12. Dispersion relation for different *Ra*.
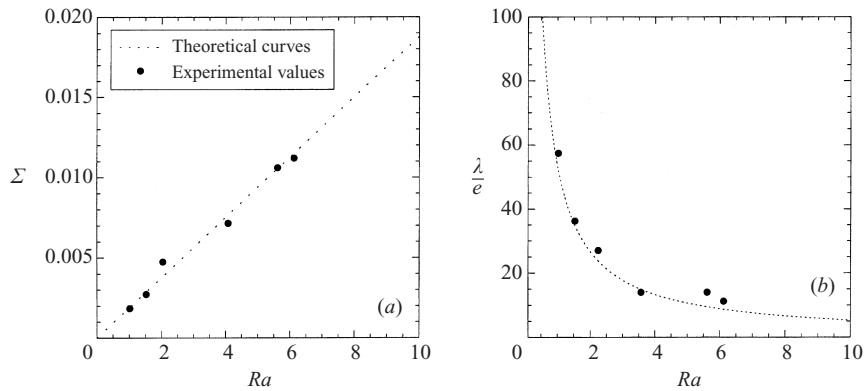
FIGURE 13. Comparison of experimental and theoretical data, (*a*) Σ versus *Ra*, (*b*) λ/e versus *Ra*.

This equation gives a maximum growth rate Σ_m and a corresponding wavenumber q_m:

$$q_m = \frac{(\sqrt{5}-2)}{2}Ra \approx 0.12\,Ra, \qquad (4.4)$$

$$\Sigma_m = \frac{(\sqrt{5}-2)(3-\sqrt{5})}{8}Ra \approx 0.0225\,Ra. \qquad (4.5)$$

The experimental and the theoretical values are in good agreement (figure 13) for the prediction of the wavelength ($\lambda/e \propto Ra^{-1}$) as well as the growth rate ($\Sigma \propto Ra$). The diffusion coefficient D can be deduced when the two curves collapse. In this case, both panels of figure 13 yield $D = 2 \times 10^{-5}\text{cm}^2\,\text{s}^{-1}$, which is a very reasonable value.

An experimental dispersion relation can be obtained from direct measurements of wavelength and growth rate, in order to compare with the results of linear stability
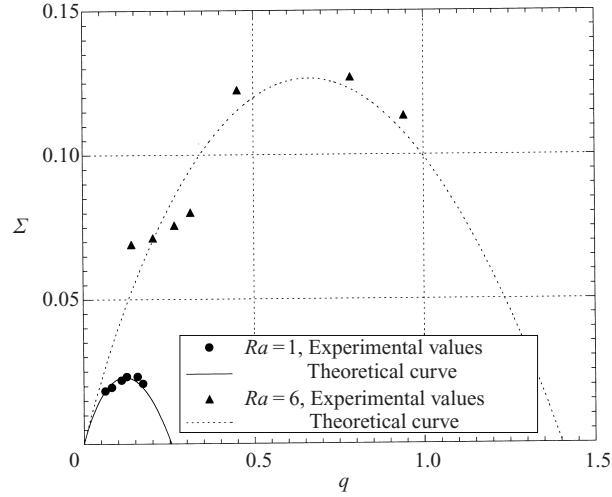
FIGURE 14. Comparison of the normalized dispersion relations for two values of Ra (1, 6) in the diffusive regime. The results from the linear stability analysis based on the Hele-Shaw equations are in good agreement with the experiments in this range of Ra values ($Ra < 10$).

theory. Soon after the instability begins in the experiment, several independent modes appear in the Fourier spectrum of the interface (figure 4). At this early stage of the interfacial instability growth, these modes do not interact with each other, and we can measure their respective growth rates. Figure 14 shows an experimental dispersion relation. For comparison purposes, the theoretical dispersion relation (4.3) is also represented in this graph. Excellent agreement is observed. It has not been possible to perform a similar comparison in the high-Ra regime, since the different modes do not remain independent for a sufficiently long time.

5. Numerical simulations

5.1. *Set of governing equations and dimensionless parameters*

We will describe both two- and three-dimensional numerical simulations of the problem, based on the Stokes equations, which in dimensional form are

$$\nabla \cdot \boldsymbol{u} = 0, \tag{5.1a}$$

$$\nabla p = \mu \nabla^2 \boldsymbol{u} - \rho g \nabla y, \tag{5.1b}$$

$$\frac{\partial c}{\partial t} + \boldsymbol{u} \cdot \nabla c = D \nabla^2 c, \tag{5.1c}$$

With the characteristic quantities introduced above, we obtain their dimensionless counterparts as

$$\nabla \cdot \boldsymbol{u} = 0, \tag{5.2a}$$

$$\nabla p = \tfrac{1}{12} \nabla^2 \boldsymbol{u} - c \nabla y, \tag{5.2b}$$

$$\frac{\partial c}{\partial t} + \boldsymbol{u} \cdot \nabla c = \frac{1}{Ra} \nabla^2 c. \tag{5.2c}$$

5.2. *Computational approach*

In the experiment, the flow field comprises many instability wavelengths, and it extends several hundred gap widths in the vertical and horizontal directions. In contrast, the simulations focus on the evolution of one or very few structures, so that the computational control volume can be of significantly smaller extent, with horizontal and vertical dimensions L_x and L_y typically of $O(5$–$10)$ and $O(10$–$40)$ gap widths, respectively. In order to minimize the effects of the smaller computational domain, we assume symmetry boundary conditions for the velocity components both in the x- and in the y-direction. Along the two plates separated by the narrow gap, all velocity components are assumed to vanish identically. In the light of these boundary conditions, it is clear that the simulations can be expected to reproduce the experiments only as long as the fingers are sufficiently far away from the upper and lower boundaries. In order to specify boundary conditions for the concentration, we can thus assume to have the pure fluids at the upper and lower boundaries. In summary, we have

$$x = \pm 0.5 L_x : \qquad u = 0, \qquad v_x = 0, \qquad w_x = 0, \qquad c_x = 0, \qquad (5.3a)$$

$$y = 0.5 L_y : \qquad u_y = 0, \qquad v = 0, \qquad w_y = 0, \qquad c = 1, \qquad (5.3b)$$

$$y = -0.5 L_y : \qquad u_y = 0, \qquad v = 0, \qquad w_y = 0, \qquad c = 0, \qquad (5.3c)$$

$$z = \pm 0.5 : \qquad u = 0, \qquad v = 0, \qquad w = 0, \qquad c_z = 0. \qquad (5.3d)$$

By taking the curl of the Stokes equation and introducing the vorticity

$$\nabla \times \boldsymbol{u} = \boldsymbol{\omega} \equiv (\xi, \eta, \zeta)^T, \qquad (5.4)$$

the above relationships can be recast in the vorticity–velocity formulation (Fletcher 1988), so that we obtain

$$\nabla^2 \boldsymbol{\omega} = 12(-c_z, 0, c_x), \qquad (5.5a)$$

$$\nabla^2 \boldsymbol{u} = -\nabla \times \boldsymbol{\omega}, \qquad (5.5b)$$

$$\frac{\partial c}{\partial t} + \boldsymbol{u} \cdot \nabla c = \frac{1}{Ra} \nabla^2 c \qquad (5.5c)$$

The above boundary conditions for the velocity components translate into the following set of conditions for the vorticity components:

$$x = \pm 0.5 L_x : \qquad \xi_x = 0, \qquad \eta = 0, \qquad \zeta = 0, \qquad (5.6a)$$

$$y = \pm 0.5 L_y : \qquad \xi = 0, \qquad \eta_y = 0, \qquad \zeta = 0, \qquad (5.6b)$$

$$z = \pm 0.5 : \qquad \xi = -v_z, \qquad \eta = u_z, \qquad \zeta = 0. \qquad (5.6c)$$

Our initial concentration profile $c_0(y)$ is taken from the family of one-dimensional solutions describing the self-similar diffusive decay of a step profile

$$c_0(y) = 0.5 + 0.5 \,\mathrm{erf}\left(\frac{y}{\delta}\right). \qquad (5.7)$$

Here, the initial profile thickness is determined by the parameter δ. In order to trigger the growth of a finger, we impose a small-amplitude perturbation on the initial interface location.

The numerical simulations are performed on grids that are equidistant in all three directions. Temporal discretization is accomplished by an explicit third-order-accurate low-storage Runge–Kutta time integration scheme to update the concentration field (Wray 1991). Spatial derivatives are discretized spectrally in the x- and y-directions,
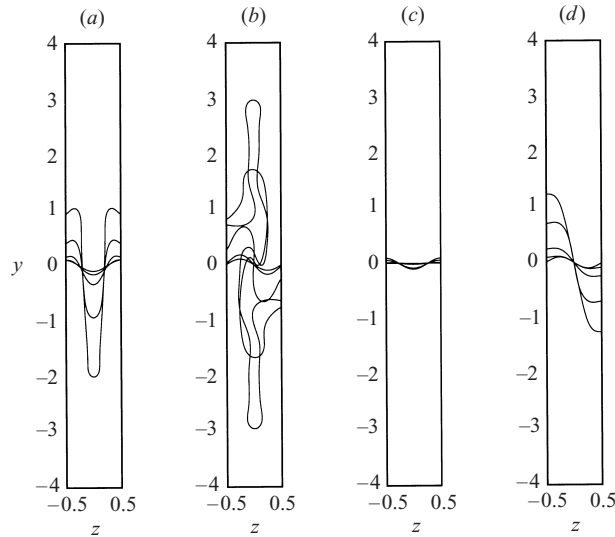
FIGURE 15. Two-dimensional simulations of the flow in the gap. For all cases shown, the interface thickness parameter $\delta = 1$ and the initial interfacial waviness has an amplitude of 0.1. The $c = 0.5$ concentration contour is shown at times 8.33×10^{-2}, 4.17, 16.7, 41.7, and 83.3. (a) $Ra = 2.5 \times 10^3$, initial perturbation is of cosine shape. (b) $Ra = 2.5 \times 10^3$, initial perturbation is of sine shape. (c) $Ra = 2.5 \times 10^2$, initial perturbation is of cosine shape. d) $Ra = 2.5 \times 10^2$, initial perturbation is of sine shape.

with the velocity and vorticity components, as well as the concentration field, expanded into sine and cosine series (Gottlieb & Orzsag 1977; Canuto *et al.* 1988). In the z-direction, we employ compact finite differences in the form given by Lele (1992), which are of sixth order in the interior of the flow domain. The evaluation of the nonlinear terms at each time level is performed in a pseudo-spectral manner (cf. Canuto *et al.* 1988). The code was validated by comparing the growth rates observed for small-amplitude perturbations with the exact results obtained from a numerical linear stability analysis (Graf, Meiburg & Härtel 2002).

5.3. *Two-dimensional flow in the gap*

As a preliminary step, we present the results of purely two-dimensional flow simulations in the narrow gap, i.e. without any variations in the spanwise direction. The computational domain extends from -4 to 4 in the y-direction, and from -0.5 to 0.5 in the z-direction. This domain is discretized into 256×32 intervals. The initial interface thickness is given by $\delta = 1$, and the initial perturbation of the interface has the form of a sine or cosine wave with amplitude 0.1, respectively.

The results are seen to depend strongly on the value of Ra. Figure 15(*a*) shows the case of $Ra = 2.5 \times 10^3$ and a cosine shaped initial disturbance. The unstable stratification is seen to give rise to a finger of the heavier fluid that propagates downward along the centre of the gap. Since there is no net flow in the vertical direction, and since the flow remains symmetric with respect to the gap centreplane, continuity requires that the lighter fluid flows upward in narrow layers between the finger and the walls.

If the initial perturbation has the shape of a sine wave instead of a cosine wave, the flow proceeds quite differently, cf. figure 15(*b*). Initially, the lighter fluid rises near one wall, while the heavier fluids sinks near the opposite wall. Soon, however,

these emerging fingers separate from the wall and proceed along the centre of the gap, which seems to be a more stable configuration. Regardless of the form of the perturbation, at this relatively large value of Ra diffusion is too weak to stabilize the interface, so that a large-scale convection process evolves within the gap. This mechanism clearly cannot be captured by the gap-averaged Hele-Shaw theory, and it explains why the experimental observations for large Ra do not follow the classical Hele-Shaw scaling laws.

For $Ra = 10^2$, both sine and cosine waves are stable, so that all initial disturbance waves are damped and the flow returns to rest, with the interface thickness growing solely as a result of diffusion. This corresponds to the low-Ra regime observed in the experiments, and it reflects a stabilizing effect of the sidewalls that is similar to observations in Rayleigh–Bénard convection problems. An interesting transitional regime exists at intermediate values of Ra. For $Ra = 2.5 \times 10^2$ the simulations show the cosine wave to be stable (figure 15c), whereas the sine wave is unstable, cf. figure 15(d). As a result, fingers do not form in the centre of the gap, and instead the fluids rise and sink along opposite walls. This finding is in agreement with the shape of the most amplified eigenfunction obtained from linear stability theory (Graf *et al.* 2002).

The above observations suggest that for $Ra \leqslant O(10^2)$ the two-dimensional density profile in the gap is stable. The exact threshold value of Ra depends on the interface thickness. As a result, the experimentally observed instability at low Rayleigh number values cannot be driven by vorticity in the spanwise x-direction. Instead, it needs to feed on vorticity aligned in the z-direction, i.e. across the gap. The concentration field will hence stay essentially uniform across the gap, so that the velocity profile will remain nearly parabolic. As a result, the depth-averaged Hele-Shaw equations should be applicable to these low-Ra flows, and we can refer to the low Rayleigh number instability in the spanwise direction as the Hele-Shaw mode.

At large Ra, the two-dimensional density profile within the gap is unstable. This instability results in the formation of spanwise vorticity that drives the formation of fingers propagating along the gap. This instability, which we will refer to as the gap mode, can have a wavy spanwise modulation, i.e. a fully three-dimensional character, so that it can lead to the formation of vorticity across the gap as well. Consequently, the three-dimensional form of the gap instability can potentially result in the formation of the experimentally observed fingers in the spanwise direction. At high Ra, we thus expect a competition between the Hele-Shaw mode and the gap mode. Which one of these modes governs the characteristics of the evolving fingers will depend on their respective growth rates. Detailed quantitative information on dispersion relationships and eigenfunctions is provided in a companion paper (Graf *et al.* 2002).

5.4. *Three-dimensional flow*

5.4.1. *The high-Ra 'gap' mode*

In the following, we investigate the high-Ra 'gap' mode by means of a fully three-dimensional simulation for $Ra = 2.5 \times 10^3$. The initial interfacial thickness is again set to $\delta = 1$. A small-amplitude cosine-shaped perturbation is introduced in the spanwise direction, which triggers the three-dimensional evolution. In order to duplicate the experimental conditions as closely as possible, we prescribe its wavelength as five times the gap width. The control volume comprises one wavelength in the spanwise direction, and it extends to ± 5 in the vertical y-direction. The simulation employs $65 \times 129 \times 33$ gridpoints in the x-, y-, and z-directions, respectively.
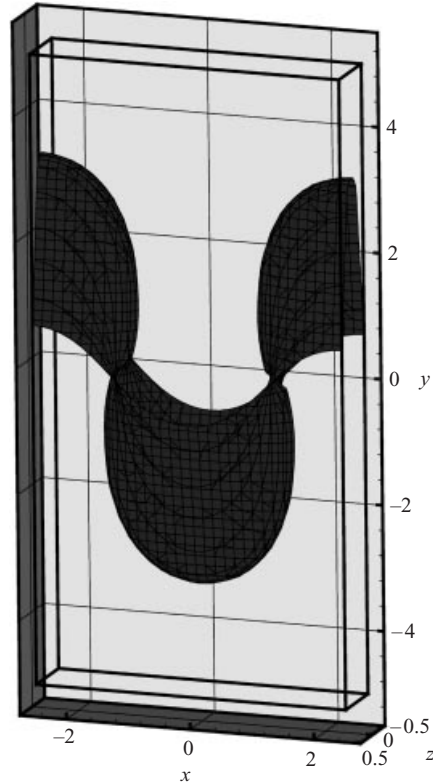
FIGURE 16. $Ra = 2.5 \times 10^3$: simulation of the three-dimensional variant of the high-Ra 'gap' mode. The interface thickness parameter $\delta = 1$, and the initial perturbation amplitude is 0.1. The $c = 0.5$ concentration contour is shown at $t = 15$. The interface exhibits a strong three-dimensional deformation.

Figure 16 depicts a perspective view of the $c = 0.5$ contour at an advanced time. We notice that at this large Rayleigh number value the concentration contour exhibits a strong deformation in the cross-gap direction, in line with the two-dimensional simulation for the same value of Ra. While this reflects the growth of the gap instability mode, its evolution is now clearly three-dimensional, with a single downward protrusion emerging in the centre of the domain, surrounded by two upward bulges in the spanwise x-direction. Note that, in contrast to the two-dimensional case, a perturbation in the cross-gap direction does not have to be prescribed here, as the spanwise wave is sufficient to trigger the flow. It is interesting that for all times the shape of the interface remains symmetrical with respect to the gap centreplane, i.e. the fingers propagate along the centreline of the gap. At the present large Rayleigh number values, diffusive effects are quite small as far as the concentration field is concerned. In conjunction with the no-slip velocity boundary condition at the walls of the cell, this causes the $c = 0.5$ contour to remain 'anchored' at its initial wall location.

5.4.2. *The low-Ra 'Hele-Shaw' mode*

At lower values of Ra a different picture emerges for the three-dimensional evolution. This is illustrated by means of a simulation for $Ra = 25$ and a perturbation wavelength of 4π times the gap width, which again closely duplicates the experi-
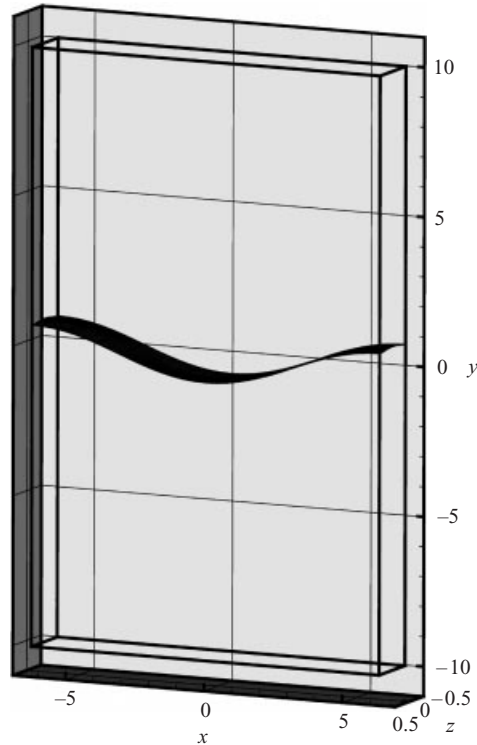
FIGURE 17. $Ra = 25$: simulation of the low-Ra 'Hele-Shaw' mode. The interface thickness parameter $\delta = 1$, and the initial perturbation amplitude is 0.1. The $c = 0.5$ concentration contour is shown at $t = 15$. The interface remains largely two-dimensional.

mentally observed conditions at the corresponding value of Ra. Figure 17 displays the $c = 0.5$ contour at an advanced time. Its lack of deformation in the cross-gap direction indicates that the concentration field stays nearly uniform across the gap, which in turn implies that the velocity field remains close to parabolic, and essentially of Hele-Shaw type. Under these conditions, the growth of the fingers can feed only on vorticity aligned in the cross-gap direction.

6. Conclusions

We have attempted to gain an understanding of density-driven instabilities between miscible fluids in a vertically arranged Hele-Shaw cell across the entire range of Ra. To this end, we applied experimental and computational tools. By means of optical measurements, we were able to extract detailed information regarding both the growth rates and the dominant wavelength from a careful analysis of the early instability phase. For the low-Ra regime, it was even possible to obtain the entire dispersion relationship experimentally. These experimental data demonstrate that in the low-Ra regime the dominant wavelength scales with Ra^{-1}, while in the large-Ra regime the length scale of the instability is 5 ± 1 times the gap width. Fully nonlinear simulations of the two- and three-dimensional Stokes equations confirm a qualitative difference between the instability modes dominating the low- and high-Ra regimes, respectively. They indicate that in the large-Ra regime a 'gap' instability mode evolves, whereas in the small-Ra regime a spanwise 'Hele-Shaw' mode dominates. Interestingly, the
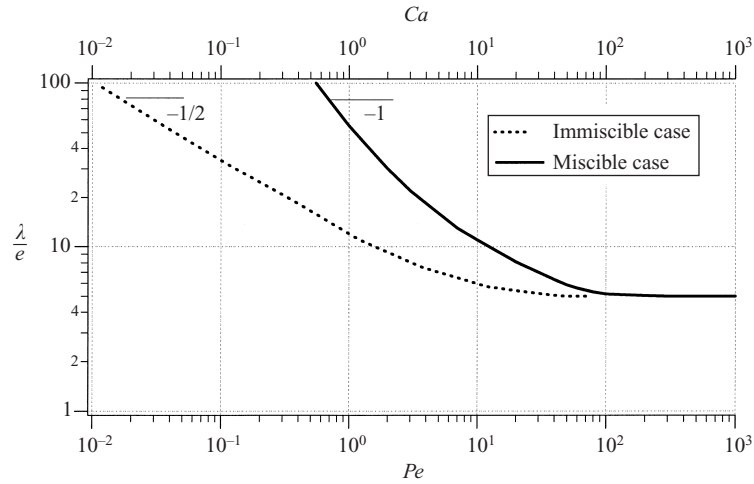
FIGURE 18. Comparison of λ/e for the viscous instability of immiscible fluids and for the gravitational instability between miscible fluids. In both cases, the curves represent fits to experimental data.

stability results of Fernandez *et al.* (2001), which are based on the Brinkman equation, capture the experimentally observed trend across the entire *Ra* range. This is perhaps somewhat surprising, since the Brinkman equation assumes a Poiseuille-type velocity profile in the gap, which in reality does not exist for large *Ra*, as our nonlinear simulations have shown.

It is of interest to compare our findings here to observations for immiscible flows. While we were unable to find quantitative stability data for density-driven immiscible flows, the well-known correspondence between density differences and unfavourable viscosity contrasts in displacement flows (e.g. Tryggvason & Aref 1983; Homsy 1987) can serve as a basis for a comparison (e.g. Maxworthy 1989). In the limit of very large viscosity contrast, the viscously driven instability between immiscible fluids in a Hele-Shaw cell can be described by a single dimensionless parameter in the form of a capillary number

$$Ca = \frac{\mu V}{\gamma}, \tag{6.1}$$

where γ represents the surface tension coefficient. Linear stability theory (Chuoke *et al.* 1959; Saffman & Taylor 1958) predicts a most amplified wavelength that scales with $Ca^{-1/2}$. This result was confirmed experimentally by Maxworthy (1989) for small values of *Ca*, whereas at larger *Ca* values three-dimensional effects are assumed to be important, cf. also Park & Homsy (1984). Figure 18 displays the present, miscible results jointly with the immiscible ones of Maxworthy (1989). Both curves represent fits to experimental data. The behaviour at large *Ra* and at large *Ca* is quite similar, in that for both cases the wavelength scales only with the gap width.

REFERENCES

BRETHERTON, F. B. 1961 The motion of long bubbles in tubes. *J. Fluid Mech.* **10**, 166.

BRINKMAN, H. C. 1947 A calculation of the viscous force exerted by a flowing fluid on a dense swarm of particles. *Appl. Sci. Res.* A **1**, 27.

CANUTO, C., HUSSAINI, M. Y., QUARTERONI, A. & ZANG, T. A. 1988 *Spectral Methods in Fluid Mechanics*. Springer.

CHEN, C.-Y. & MEIBURG, E. 1996 Miscible displacements in capillary tubes. Part 2. Numerical simulations. *J. Fluid Mech.* **326**, 57.

CHEN, C.-Y. & MEIBURG, E. 1998 Miscible porous media displacements in the quarter five-spot configuration. Part 1. The homogeneous case. *J. Fluid Mech.* **371**, 233.

CHUOKE, R. L., VAN MEURS, P. & VAN DER POEL, C. 1959 The instability of slow, immiscible, viscous liquid-liquid displacements in permeable media. *Trans. Am. Inst. Min. Metall. Pet. Engng* **216**, 188.

DEGREGORIA, A. J. & SCHWARTZ, L. W. 1986 *J. Fluid Mech.* **164**, 383.

DEGREGORIA, A. J. & SCHWARTZ L. W. 1987 *Phys. Rev. Lett.* **58**, 1742.

FERNANDEZ, J., KUROWSKI, P., LIMAT, L. & PETITJEANS, P. 2001 Rayleigh-Taylor instability inside Hele-Shaw cells: A new approach of wavelength selection problem. *Phys. Fluids* (in press).

FLETCHER, C. A. J. 1988 *Computational Techniques for Fluid Dynamics*, vol. 2. Springer.

GOTTLIEB, D. & ORSZAG, S. A. 1977 *Numerical Analysis of Spectral Methods*. SIAM, Philadelphia.

GRAF, F., MEIBURG E. & HÄRTEL, C. 2002 Density-driven instabilities of miscible fluids in a Hele-Shaw cell: Linear stability analysis of the three-dimensional Stokes equations. *J. Fluid Mech.* **451**, 261.

HOMSY, G. M. 1987 Viscous fingering in porous media. *Annu. Rev. Fluid Mech.* **19**, 271.

KUROWSKI, P., MISBAH, C. & TCHOURKINE, S. 1995 Gravitational instablity of a fictitious front during mixing of miscible fluids. *Europhys. Lett.* **29** (4), 309.

LAJEUNESSE, E., MARTIN, J., RAKOTOMALALA, N. & SALIN, D. 1997 3D instablity of miscible displacements in a Hele-Shaw cell. *Phys. Rev Lett.* **79**, 5254.

LAJEUNESSE, E., MARTIN, J., RAKOTOMALALA, N., SALIN, D. & YORTSOS, Y. C. 1999 Miscible displacement in a Hele-Shaw cell at high rates. *J. Fluid Mech.* **398**, 299.

LAJEUNESSE, E., MARTIN, J., RAKOTOMALALA, N. SALIN, D. & YORTSOS, Y. C. 2001 The threshold of the instability in miscible displacements in a Hele-Shaw cell at high rates. *Phys. Fluids* **13**, 799.

LELE, S. K. 1992 Compact finite difference schemes with spectral-like resolution. *J. Comput. Phys.* **103**, 16.

MANICKAM, O. & HOMSY, G. M. 1993 Stability of miscible displacements in porous media with nonmonotonic viscosity profiles. *Phys. Fluids* A **5**, 1356.

MAXWORTHY, T. 1987 The nonlinear growth of a gravitational unstable interface in a Hele-Shaw cell. *J. Fluid Mech.* **177**, 207.

MAXWORTHY, T. 1989 Experimental study of interface instability in a Hele-shaw cell. *Phys. Rev.* A **39** (11), 5863.

MEIBURG, E. & HOMSY, G. M. 1988 Nonlinear unstable viscous fingers in Hele-Shaw flows. II. Numerical simulation. *Phys. Fluids* **31**, 429.

PARK, C. W. GORELL, S. & HOMSY, G. M. 1984 Two-phase displacement in Hele-Shaw cells: experiments on viscously driven instabilities. *J. Fluid Mech.* **141**, 275.

PARK, C.-W. & HOMSY, G. M. 1984 Two-phase displacements in Hele-Shaw cells: Theory. *J. Fluid Mech.* **139**, 291.

PATERSON, L. 1985 Fingering with miscible fluids in a Hele-shaw cell. *Phys. Fluids* **28**, 26.

PETITJEANS, P., CHEN, C.-Y., MEIBURG, E. & MAXWORTHY, T. 1999 Miscible quarter five-spot displacements in a Hele-Shaw cell and the role of flow-induced dispersion. *Phys. Fluids* **7**, 1705.

PETITJEANS, P. & MAXWORTHY, T. 1996 Miscible displacements in capillary tubes. Part 1. Experiments. *J. Fluid Mech.* **326**, 37.

ROGERSON, A. & MEIBURG, E. 1993a A Shear stabilization of miscible displacement process in porous media. *Phys. Fluids* A **5**, 1344.

ROGERSON, A. & MEIBURG, E. 1993b Numerical simulation of miscible displacement processes in porous media flows under gravity. *Phys. Fluids* A **5**, 2644.

Ruith, M. & Meiburg, E. 2000 Miscible rectilinear displacements with gravity override. Part 1. Homogeneous porous medium. *J. Fluid Mech.* **420**, 225.

Saffman, P. G. & Taylor, G. I. 1958 The penetration of a fluid into a porous medium or Hele-Shaw cell containing a more viscous liquid. *Proc. R. Soc. Lond.* A **245**, 312.

Schwartz, L. 1986 Stability of Hele-Shaw flows: The wetting-layer effect. *Phys. Fluids* **29**, 3086.

Sharp, D. H. 1984 An overview of Rayleigh-Taylor instability. *Physica* D **12**, 3.

Tan, C. T. & Homsy, G. M. 1986 Stability of miscible displaccements in porous media: Rectilinear flow. *Phys. Fluids* **29**, 3549.

Tan, C. T. & Homsy, G. M. 1988 Simulation of nonlinear fingering in miscible displacement. *Phys. Fluids* **31**, 1330.

Taylor, G. I. 1953 Dispersion of soluble matter in solvent flowing slowly through a tube. *Proc. R. Soc. Lond.* A **219**, 186.

Tryggvason, G. & Aref, A. 1983 Numerical experiments on Hele-Shaw flow with a sharp interface. *J. Fluid Mech.* **136**, 1.

Wooding, R. A. 1969 Growth of fingers at an unstable diffusing interface in a porous medium or Hele-Shaw cell. *J. Fluid Mech.* **39**, 477.

Wray, A. 1991 Minimal storage time-advancement schemes for spectral methods. Preprint.

Yang, Z. & Yortsos, Y. C. 1997 Asymptotic solutions of miscible displacements in geometries of large aspect ratios. *Phys. Fluids* **9**, 286.